ORIGINAL PAPER

Thermal equation of state of Cr-pyrope: implications for entrapment pressure of Cr-pyrope inclusion in diamond

Jingui Xu[1,2] · Dawei Fan[1] · Bo Li[1,3] · Sergey N. Tkachev[4] · Dongzhou Zhang[2] · Guangzhong Yang[5] · Yi Zhou[6] · Jiamei Song[1,7] · Wenge Zhou[1]

Abstract

Cr-pyrope is one of the most abundant mineral inclusions in peridotitic diamonds and its thermal equation of state (EoS) is a prerequisite for accurately determining its entrapment pressure (P_e), which is important to understanding the physicochemical environment of diamond formation. We present in situ single-crystal X-ray diffraction (XRD) experimental results of five natural Cr-pyropes (Cr# = 0.3–22.4, Cr# = Cr/(Cr + Al)) at high pressure (P), high temperature (T), and high P–T up to 13.2 GPa and 950 K. The obtained P–volume(V)–T data were used to derive EoS parameters. The results indicated that the compressional behaviors of these Cr-pyropes are close (up to 2.8% difference), but the differences between their thermal expansivities are up to 8.8%. The thermal expansivities of the Cr-pyropes are significantly higher than that of end-member garnets (pyrope, almandine, and grossular) obtained by room-P high-T XRD, but they are consistent with the end-member thermal expansivities obtained by high P–T XRD. To investigate the compositional effects on the estimation of P_e of Cr-pyrope, the obtained EoS parameters were used to calculate the P_e in diamond. The results indicated that the variation in thermal expansion behavior plays a more significant role in influencing the P_e in comparison with the compressional behavior. In addition, the P_e of the Cr-pyropes are compared with the P_e of end-member garnets (pyrope, almandine, grossular, and uvarovite), which indicates that the low-Cr (Cr# = 0.3–4.4) pyropes are closer to pyrope in P_e while the high-Cr (Cr# = 9.3–22.4) pyropes are closer to grossular.

Keywords Cr-pyrope · Thermal equation of state · Diamond · Entrapment pressure

Introduction

Some natural diamonds that have been brought to the surface contain mineral inclusions, which provide samples of the deep Earth. To investigate the formation of diamond and the composition and structure of the Earth's interior, one needs to determine the pressure/depth of the inclusion entrapment. Recently, elastic geo-barometry has been used to determine the entrapment pressure (P_e) during the growth of a diamond based on the elasticity theory (e.g., Angel et al. 2014a, 2017; Gilio et al. 2021; Milani et al. 2015). This method has

Communicated by Dante Canil.

✉ Jingui Xu
    xujingui@hawaii.edu

1 Key Laboratory for High-Temperature and High-Pressure Study of the Earth's Interior, Institute of Geochemistry, Chinese Academy of Sciences, Guiyang 550081, Guizhou, China

2 Hawai'i Institute of Geophysics and Planetology, School of Ocean and Earth Science and Technology, University of Hawai'i at Manoa, Honolulu, HI 96822, USA

3 Research Institute of Petroleum Exploration & Development-Northwest (NWGI), PetroChina, Lanzhou 730060, Gansu, China

4 Center for Advanced Radiation Sources, University of Chicago, Chicago, IL 60437, USA

5 The No. 101 Geological Brigade, Geological and Mineral Exploration and Development Bureau of Guizhou Province, Kaili 556000, Guizhou, China

6 School of Geoscience and Technology, Southwest Petroleum University, Chengdu 610500, Sichuan, China

7 University of Chinese Academy of Sciences, Beijing 100049, China

advantages in determining P_e in comparison with the other well-known method which is based on the cation distribution between coexisting phases (Nestola 2021). The elastic geo-barometry calculates the isomeke, which is a curve in the pressure (P)–temperature (T) space and defines the conditions that the void of the host (e.g., diamond in our case) and inclusion (Cr-Pyrope in our case) would have the same P, T, and volume (V). The isomeke is calculated based on the residual pressure of an inclusion (P_i) and the thermal equation of state (EoS) parameters (e.g., bulk modulus and thermal expansion coefficient) of the host and the inclusion, and represents possible entrapment conditions (e.g., Angel et al. 2017). Therefore, the thermal EoS parameters of relevant minerals (host and inclusion) are necessary for the application of this geo-barometer (Mazzucchelli et al. 2021). Thermal EoS parameters of a mineral describe how its V changes with the varying P and T and can be derived by fitting the measured P–V–T data to an established EoS.

According to the statistic by Stachel and Harris (2008), more than 1/3 of lithospheric diamonds are of peridotitic origin. Garnet is one of the most abundant minerals occurring as inclusion in peridotitic diamonds. Natural garnets, with a general formula of $X_3Y_2Si_3O_{12}$, are generally formed in multi-component solid solutions and are the result of the flexible cation substitution in both X (Mg^{2+}, Fe^{2+}, Ca^{2+}, Mn^{2+}) and Y (Al^{3+}, Fe^{3+}, Cr^{3+}) sites (e.g., Geiger 2008; Grew et al. 2013). Garnet inclusions in peridotitic diamonds are Cr-pyropes, and their Cr_2O_3 contents vary from ~ 1 wt.% to larger than 20 wt.% (Stachel and Harris 2008). Natural Cr-pyropes are mainly composed of pyrope (Prp_{100}; $Mg_3Al_2Si_3O_{12}$), almandine (Alm_{100}; $Fe_3Al_2Si_3O_{12}$), grossular (Grs_{100}; $Ca_3Al_2Si_3O_{12}$), uvarovite (Uvr_{100}; $Ca_3Cr_2Si_3O_{12}$), knorringite (Knr_{100}; $Mg_3Cr_2Si_3O_{12}$), andradite (Adr_{100}; $Ca_3Fe_2^{3+}Si_3O_{12}$) and spessartine (Sps_{100}; $Mn_3Al_2Si_3O_{12}$), the last two of which are usually very minor (Stachel and Harris 2008).

The thermal EoS of diamond has been well established by literature studies (e.g., Angel et al. 2015; Dewaele et al. 2008; Gillet et al. 1999; Prencipe et al. 2014), but the thermal EoS parameters of Cr-pyrope are still lacking for accurately determining P_e of Cr-pyrope inclusions in diamond using elasticity geo-barometry. To date, numerous studies have been performed on the EoS (P–V, T–V or thermal EoS) and elasticity of Prp_{100} (e.g., Chantel et al. 2016; Chen et al. 1999; Du et al. 2015; Fan et al. 2019; Levien et al. 1979; Milani et al. 2015; Wang and Ji 2001), Alm_{100} (Arimoto et al. 2015; Conrad et al. 1999; Milani et al. 2015), Grs_{100} (Bass 1989; Milani et al. 2017), Uvr_{100} (Bass 1986; Fan et al. 2015; Gréaux and Yamada 2019), some binary [Prp-Alm (Huang and Chen 2014), Prp-Grs (Du et al. 2015) and Grs-Adr (Fan et al. 2017; Wei et al. 2021)] and Prp-Alm-Grs ternary (Beyer et al. 2021; Chai et al. 1997; O'Neill et al. 1989; Xu et al. 2019). Studies on the EoS of Knr_{100} are still

unavailable as Knr_{100} synthesized from pure $Mg_3Cr_2Si_3O_{12}$ always contained a significant amount of majorite (Maj; $Mg_4Si_4O_{12}$) component (Dymshits et al. 2014; Zou and Irifune 2012). Studies on thermoelastic properties of Cr-pyrope are very limited (Babuška et al. 1978; Suzuki and Anderson 1983). Babuška et al. (1978) measured the elastic properties of four Cr-pyropes ($Cr_2O_3 < 3$ wt.%; Mg# = 81–84 and Cr# = 5–9; Mg# = Mg/(Mg + Fe) and Cr# = Cr/(Cr + Al)) by means of the rectangular parallelepiped resonance (RPR) method at room P–T. Using the same method, Suzuki and Anderson (1983) investigated a natural Cr-pyrope (Mg# = 82 and Cr# = 6) to 1000 K at room P. To the best of our knowledge, there are still no thermal EoS studies of Cr-pyrope at high P–T.

As an analogy to the Vegard's law for volume–composition relationship, the bulk modulus of garnet solid solution is often considered to be calculated from the bulk moduli of its end members assuming a linear relationship between composition and bulk modulus (e.g., Beyer et al. 2021; Ita and Stixrude 1992; O'Neill et al. 1989), although some studies suggested that bulk modulus of a solid solution containing grossular could be nonlinearly dependent on varying composition (Du et al. 2015; Xu et al. 2019). However, the compositional effects on the thermal EoS of Cr-pyrope have not yet been investigated. In this study, we report synchrotron-based single-crystal X-ray diffraction (SCXRD) measurements on five natural Cr-pyropes with various Cr_2O_3 contents (0.1–7.3 wt.%) at high P and high T to ~ 13 GPa and 950 K, from which complete thermal EoS parameters are extracted. The compositional effects on the thermal EoS parameters are discussed. We apply the obtained thermal EoS parameters of Cr-pyrope to the diamond–garnet geo-barometry to investigate the effects of thermal EoS parameters on the P_e of Cr-pyrope.

Sample and methods

Five natural Cr-pyropes used in this study are collected from lamproite in Zhenyuan, Guizhou Province, China. We chose several grains (hundreds of micrometers) for each Cr-pyrope for electron microprobe analyses (EMPA). These grains were first placed at the bottom of a cylindrical vessel (~ 20 mm in diameter), then the vessel was filled with freshly mixed epoxy and vacuum degassed. After the epoxy was cured, the epoxy plug was taken out of the vessel and was polished and carbon-coated for the final EMPA analyses. The EMPA analyses were carried out with a JXA 8230, operating at an acceleration voltage of 25 kV, beam current of 10 nA, and focused electron beam of approximately 5 μm. Counting times were 10 on the peak and 5 s on the background for each element. Natural pyrope was used as the standard for Fe, Mn, Ti, Cr, Si, Al, Mg and Ca, olivine for Ni, albite

for Na, and orthoclase for K. Analyzing crystal was LIFH for Fe, Ni, and Mn, PETJ for Ti and Cr, TAP for Na, Si, Al, and Mg, and PETH for K and Ca. The results are shown in Table S1, and the compositions of these five Cr-pyropes expressed in end-member molar percentages are shown in Table 1. The end-member proportions were calculated according to the method proposed by Locock (2008). The Fe^{3+} contents were estimated based on the charge balance. For simplicity, we designate these five garnets Prp-Cr#0.3, Prp-Cr#4.4, Prp-Cr#9.3, Prp-Cr#15.1, and Prp-Cr#22.4 in turn. Prp-Cr#3.5, Prp-Cr#9.3, Prp-Cr#15.1, and Prp-Cr#22.4 have similar compositions as the Cr-pyropes found as inclusions in peridotitic diamonds (Fig. 1). Backscattered electron (BSE) images reveal that these garnets are not zoned into different chemical domains (Figure S1) and that Prp-Cr#15.1 contains several inclusions. The crystals used for SCXRD were inclusion-free and of high diffraction quality.

Three runs of SCXRD experiments were conducted for these Cr-pyropes. In the first run (run #1), room-T high-P SCXRD was performed to 9.5 GPa. In run #2, the SCXRD data were collected at high P–T up to 13 GPa and 700 K. The room-P high-T experiments from room T up to 950 K were performed in run #3. One crystal was used for each Cr-pyrope in each run.

In run #1, a BX90 diamond anvil cell (DAC) equipped with two 500-µm-culet diamonds and WC seats was used; an externally heated DAC was used in run #2, which was the same DAC used in run #1 but equipped with a micro-resistive heater made from alumina ceramic and coiled Pt wires and a K-type thermocouple attached to one of the diamond anvils approximately 500 µm away from the culet. In run #1 and run #2, a rhenium gasket was pre-indented to a thickness of ~60 µm by the diamond anvils, and a 350-µm hole was subsequently laser drilled on the indented area and was used as the sample chamber. A gold foil and five crystals (square (irregular) shape with side lengths of 30–60 µm and thicknesses of 10–15 µm) were loaded together into the sample chamber (Figure S2) followed by gas-loading with neon as the pressure medium using the COMPRES/GSECARS gas-loading system (Rivers et al. 2008). The pressure was measured using the EoS of gold (Dorogokupets and Dewaele
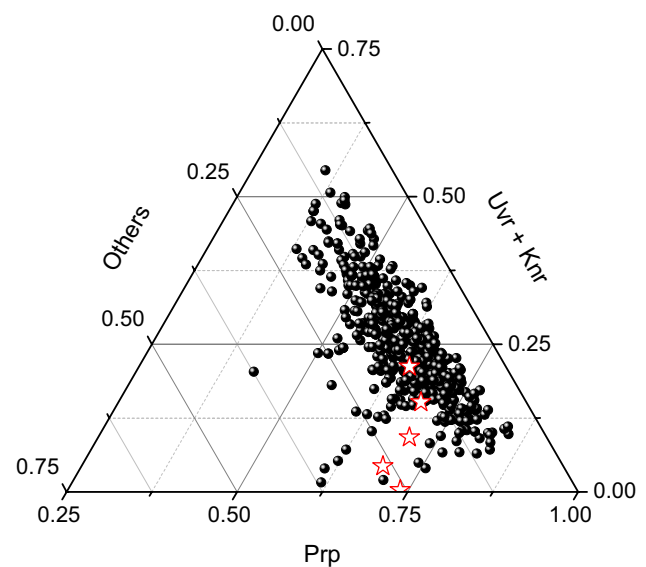

Fig. 1 End-member proportions of Cr-pyrope inclusions found in diamonds (black ball) and of the five Cr-pyropes in this study (red star). Prp = pyrope ($Mg_3Al_2Si_3O_{12}$); Uvr = uvarovite ($Ca_3Cr_2Si_3O_{12}$); Knr = Knorringite ($Mg_3Cr_2Si_3O_{12}$). Other end members include almandine ($Fe_3Al_2Si_3O_{12}$), grossular ($Ca_3Al_2Si_3O_{12}$), andradite ($Ca_3Fe^{3+}_2Si_3O_{12}$), schorlomite-Al ($Ca_3Ti_2Al_2SiO_{12}$), morimotoite ($Ca_3TiFe^{3+}Si_3O_{12}$), majorite ($Mg_4Si_4O_{12}$), spessartine ($Mn_3Al_2Si_3O_{12}$), and skiagite ($Fe_3Fe^{3+}_2Si_3O_{12}$). Data for Cr-pyrope inclusions are from previous studies Banas et al. (2007, 2009), Chi (1996), Davies et al. (2004a, b), Deines et al. (1991), Deines and Harris (2004), Donnelly et al. (2007), Griffin et al. (1993, 2001), Harris et al. (2004), Hunt et al. (2012), Koornneef et al. (2017), Kopylova et al. (1997), Kurat and Dobosi (2000), Meyer and Svisero (1975), Miller et al. (2012, 2014), Ntanda et al. (1982), Phillips et al. (2004), Prinz et al. (1975), Qi et al. (1999), Schulze et al. (2008), Shatsky et al. (2015), Sobolev et al. (2004, 2009), Stachel and Harris (1997), Stachel et al. (1998, 2000, 2003, 2004a, b, 2006), Tappert et al. (2005a, b, 2006), Taylor et al. (2003, 2016), Viljoen et al. (2014), Wang et al. (2000), Wang and Guo (1994), Wiggers de Vries et al. (2013), Zedgenizov et al. (2016), Zhang (1991). The data of Cr-pyrope inclusions are available in the supplementary

2007). In run #3, each sample was loaded into a fused silica capillary with a 100 µm inner diameter, and nearly cubic crystals (~100-µm side lengths) were used. The sample temperature was achieved by helium flow heated with a tungsten

Table 1 End-member molar percentage of the Cr-pyropes in this study

Sample	Pyrope	Almandine	Grossular	Andradite	Spessartine	Uvarovite	Knorringite	Schorlomite-Al	Skiagite
Prp-Cr#0.3	73.9	15.5	7.7	1.3	0.4	0.3	0.0	0.8	0
Prp-Cr#4.4	69.3	17.6	7.4	0.2	0.7	4.4	0.0	0.4	0
Prp-Cr#9.3	70.6	15.7	3.1	0.5	0.6	9.2	0.0	0.3	0
Prp-Cr#15.1	69.1	14.8	0.3	0.0	0.6	15.1	0.0	0.1	0
Prp-Cr#22.4	64.3	13.2	0.0	0.0	0.6	16.0	5.1	0.2	0.6

Pyrope $Mg_3Al_2Si_3O_{12}$, *Almandine* $Fe_3Al_2Si_3O_{12}$, *Grossular* $Ca_3Al_2Si_3O_{12}$, *Andradite* $Ca_3Fe^{3+}_2Si_3O_{12}$, *Spessartin* $Mn_3Al_2Si_3O_{12}$, *Uvarovite* $Ca_3Cr_2Si_3O_{12}$, *Knorringite* $Mg_3Cr_2Si_3O_{12}$, *Schorlomite-Al* $Ca_3Ti_2Al_2SiO_{12}$, *Skiagite* $Fe_3Fe^{3+}_2Si_3O_{12}$

heater (Zhang et al. 2021), and a K-type thermocouple was used to monitor the temperature.

Run #1 and run #2 were performed at the 13-BM-D station of the Advanced Photon Source (APS), Argonne National Laboratory (ANL). The incident X-ray had a wavelength of 0.3344 Å and a beam size of 3×7 μm². The diffraction images were acquired using a stationary Perkin-Elmer area detector. At each P–T, a series of ω-scan steps, with one-degree step and exposure time of 5 s/°, were collected. The range of the ω-rotation was 30 °. The ω rotation axis was vertical and perpendicular to the incident beam. Run #3 was performed at the 13-BM-C experimental station of APS, ANL. The incident X-ray beam at 13-BM-C was monochromated to 0.4340 Å with a focal spot size of 12×18 μm² (Xu et al. 2022; Zhang et al. 2017). The SCXRD was carried out with a six-circle diffractometer and a Pilatus3 1 M Si detector. Stepped φ exposures were collected at each P–T point with an exposure time of 0.5 s/°, and the φ scan rotation axis was horizontal and perpendicular to the incident X-ray direction. In all these three runs, LaB₆ was used as the diffraction standard. The diffraction images (Fig. S3) collected in run #1 and run #2 were analyzed with the ATREX software package (Dera et al. 2013), while the Bruker APEX3 software suite was used for the diffraction images collected in run #3. The obtained unit-cell parameters of each Cr-pyrope are shown in Table S2.

Results

Room-*T* *P*–*V* EoS

At room-*T*, the unit-cell volume of each of the five Cr-pyropes decreased smoothly with increasing pressure up to 9.5 GPa without indication of phase transitions (Fig. 2a). To obtain the EoS parameters, we fit the *P*–*V* data to a third-order Birch–Murnaghan (BM3; Birch (1947)) EoS using the Eosfit7 package (Angel et al. 2014b; Gonzalez-Platas et al. 2016). The resulting EoS parameters including zero-*P* unit-cell volume (V_{T0}), zero-*P* isothermal bulk modulus (K_{T0}), and its pressure derivative (K'_{T0}) are reported in Table 2. As a comparison, the *P*–*V* data were also fitted to a third-order Tait EoS (Freund and Ingalls 1989; Holland and Powell 2011), which shows that the Tait EoS and BM3 EoS fitting yield indistinguishable EoS parameters within the uncertainty. The obtained V_{T0}, K_{T0} and K'_{T0} are within 1529.1(2)-1551.8(3) Å³, 165.4(27)–170.2(35) GPa and 3.9(9)–5.1(9), respectively. As shown in Fig. 2a, the EoS fit represents the *P*–*V* data very well for each Cr-pyrope. The f_E–F_E plot (Angel 2000) was used for better visualization of the quality of the EoS fit. As shown in Fig. 2(b-f), for Prp-Cr#0.3, Prp-Cr#4.4, Prp-Cr#9.3 and Prp-Cr#15.1, the f_E–F_E data points lie on

a horizontal line, indicating a K'_{T0} value very close to 4; while the f_E–F_E data of Prp-Cr#22.4 lie on an inclined line with a positive slope which indicates a K'_{T0} value larger than 4. Thus, the f_E–F_E plot is consistent with our BM3 EoS parameters.

Thermal EoS

We used an isothermal EoS model (Text S1) to fit the *P*–*V*–*T* data (Fig. 3(a-e)) by combining the BM3 EoS with the Fei-type (Fei 1995) thermal expansion model, and the temperature derivative of the bulk modulus ($(\partial K_T/\partial T)_P$; (Angel et al. 2014b). The V_{T0}, K_{T0} and K'_{T0} were fixed at the value obtained from the room-*T* EoS fitting when we performed the thermal EoS fitting. The results are reported in Table 3, showing $\alpha_0 = 2.65(9)$–$3.41(9) \times 10^{-5}$ K^{-1}, $\alpha_1 = -0.05(8)$–$1.41(11) \times 10^{-8}$ K^{-2}, $\alpha_2 = -0.75(9)$–$-0.03(6)$ K, and $(\partial K_T/\partial T)_P = -0.031(4)$– $-0.019(3)$ GPa/K. Figure 3a–e indicates a good thermal EoS fit to the high *P*–*T* data for each Cr-pyrope.

Helffrich and Connolly (2009) suggested that using a constant $(\partial K_T/\partial T)_P$ in thermal EoS fitting could lead to the prediction of non-physical thermal expansion at high pressures, thus they proposed an equation (HC2009) to describe the temperature effects on K_{T0} (Text S1) using the Anderson–Grüneisen parameter (δ). Therefore, we also fitted our *P*–*V*–*T* data to the isothermal EoS model described in the preceding paragraph, but the HC2009 equation instead of the $(\partial K_T/\partial T)_P$ was used for the variation of bulk modulus with temperature. The EoS fit yielded $\delta = 3.83(68)$–$5.53(74)$, $\alpha_0 = 2.65(9)$–$3.40(9) \times 10^{-5}$ K^{-1}, $\alpha_1 = -0.05(8)$–$1.41(11) \times 10^{-8}$ K^{-2}, and $\alpha_2 = -0.75(9)$ to $-0.04(6)$ K. The results are also shown in Table 3, indicating that using the HC2009 equation did not yield much difference in the EoS parameters in comparison to using the linear relationship between K_{T0} and temperature.

We also used the thermal-pressure EoS (Text S2) proposed by Holland and Powell (2011) to fit the *P*–*V*–*T* data. The Einstein temperature (θ_E) of the Cr-pyropes was calculated according to the method described by Holland and Powell (2011), yielding $\theta_E = 508$–522 K. Again, the V_{T0}, K_{T0} and K'_{T0} were fixed at the value obtained from the room-*T* EoS fitting when we performed the thermal EoS fitting. The obtained EoS parameters are shown in Table 3, and the thermal expansion coefficients at 300 K (α_{300}) are $2.568(4)$–$2.908(3) \times 10^{-5}$ K^{-1}. The isotherms generated using these EoS parameters are also shown in Fig. 3a–e, showing good EoS fit for each Cr-pyrope.

The input and output files for each EoS fitting are available in the supplementary.
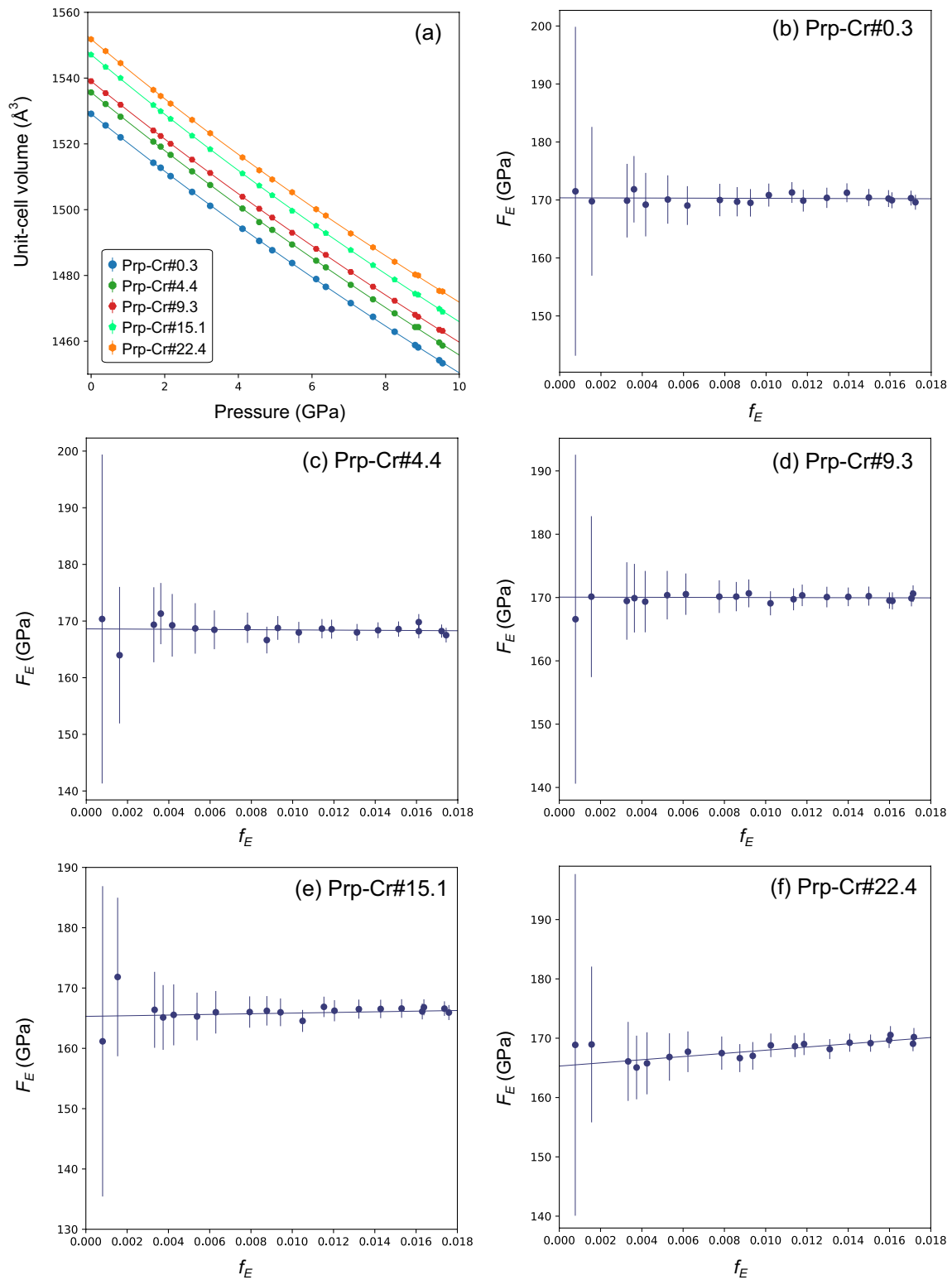
Fig. 2 a The unit-cell volume of the five Cr-pyropes as a function of pressure. **b–f** f_E–F_E plot for each Cr-pyrope. The solid lines represent the BM3 EoS fitting for the data. Error bars may be smaller than the symbol size

Table 2 Zero-pressure volume (V_{T0}), isothermal bulk modulus (K_{T0}) and its pressure derivative (K'_{T0}) of the Cr-Pyropes

	V_{T0} (Å^3)	K_{T0} (GPa)	K'_{T0}
Prp-Cr#0.3[a]	1529.1(2)	170.2(35)	4.0(9)
Prp-Cr#0.3[b]	1529.1(2)	170.2(35)	4.0(9)
Prp-Cr#4.4[a]	1535.6(2)	168.7(35)	3.9(9)
Prp-Cr#4.4[b]	1535.6(2)	168.7(35)	3.9(9)
Prp-Cr#9.3[a]	1539.1(2)	170.0(35)	4.0(9)
Prp-Cr#9.3[b]	1539.1(2)	170.0(35)	4.0(9)
Prp-Cr#15.1[a]	1547.1(3)	165.7(35)	4.2(9)
Prp-Cr#15.1[b]	1547.1(3)	165.7(35)	4.2(9)
Prp-Cr#22.4[a]	1551.8(3)	165.4(37)	5.1(9)
Prp-Cr#22.4[b]	1551.8(3)	165.4(37)	5.1(9)

[a]BM3 EoS

[b]Third-order Tait EoS

Discussion

Comparing the EoS results of these five Cr-pyropes indicates that the compositional effects are very limited for K_{T0} and K'_{T0}. As shown in Table 2, the K_{T0} of Prp-Cr#0.3, Prp-Cr#4.4, and Prp-Cr#9.3 K_{T0} are around 170 GPa (168.7(35)-170.2(35) GPa). In comparison with these three Cr-pyropes, Prp-Cr#15.1 and Prp-Cr#22.4 have only slightly smaller K_{T0} (165.4(27)–165.7(35) GPa). In addition, the K'_{T0} of Prp-Cr#0.3, Prp-Cr#4.4, Prp-Cr#9.3 and Prp-Cr#15.1 are very close to 4, while the K'_{T0} of Prp-Cr#22.4 is greater than 4 (5.1(9); Fig. 2f). The higher K'_{T0} of Prp-Cr#22.4 could be caused by the presence of a Knr component since a previous study (Dymshits et al. 2014) reported a high K'_{T0} (5.4(12)) for Knr$_{81}$Maj$_{19}$. The obtained K_{T0} of Prp-Cr#0.3, Prp-Cr#4.4, and Prp-Cr#9.3 are comparable to the K_{T0} of Cr-pyropes (Cr# = 5–9; K_{T0} = 168.3(18)-169.8(13) GPa) reported by Babuška et al. (1978) using the RPR method.

We also compared our K_{T0} with the K_{T0} of end-member garnets related to Cr-pyrope, including Prp$_{100}$, Alm$_{100}$, Grs$_{100}$ and Uvr$_{100}$ from previous studies (Fig. S4 and Table S3; Arimoto et al. 2015; Bass 1986, 1989; Chantel et al. 2016; Chen et al. 1999; Conrad et al. 1999; Diella et al. 2004; Du et al. 2015; Fan et al. 2015, 2019; Gréaux et al. 2011; Gréaux and Yamada 2019; Gwanmesia et al. 2006, 2007, 2014; Hazen and Finger 1978; Isaak et al. 1992; Kono et al. 2010; Leger et al. 1990; Leitner et al. 1980; Levien et al. 1979; Milani et al. 2015, 2017; O'Neill et al. 1991; Olijnyk et al. 1991; Pavese et al. 2001a, b; Sato et al. 1978; Sinogeikin and Bass 2000, 2002; Suzuki and Anderson 1983; Takahashi and Liu 1970; Wang et al. 1998; Wang and Ji 2001; Weaver et al. 1976; Zhang et al. 1998, 1999; Zou et al. 2012a, b). We did not include spessartine, andradite, and knorringite as they are minor components of the Cr-pyropes in this study. Prp$_{100}$ is the most studied end-member

garnet, and more than twenty studies have reported the bulk modulus of Prp$_{100}$. As shown in Figure S4 and Table S3, the results are quite scattered, from 133(3) GPa to 212(8) GPa; however, the K_{T0} obtained by direct measurements (such as Brillouin light spectroscopy (BLS), ultrasonic interferometry (UI) and RPR) are concentrated around 170 GPa. Up till now, there have been six direct measurements on Prp$_{100}$ by various methods (Chantel et al. 2016; Chen et al. 1999; Gwanmesia et al. 2006; Leitner et al. 1980; Sinogeikin and Bass 2000; Zou et al. 2012b), of which the most recent five studies came to K_{T0} = 168.5(2)–170.5(16) GPa that are lower than K_{T0} = 175(1) reported by Leitner et al. (1980).

Four XRD studies have been performed on Alm$_{100}$, and the results were within 173(2)–190(5) GPa; two UI studies have reported very close K_{T0} (172.7(10) and 173.6(9) GPa). For Grs$_{100}$, the K_{T0} reported by XRD studies was 139(5)–170.2(35) GPa. The direct measurements conducted by methods of BLS (Bass 1989; Conrad et al. 1999), UI (Wang and Ji 2001), and RPR (Isaak et al. 1992) arrived at very similar K_{T0} (165.0(27)-167.1(7) GPa), which are smaller than the K_{T0} reported by the other two UI studies (169.7(1) and 170.3(8) GPa; (Gwanmesia et al. 2014; Kono et al. 2010). In comparison to Prp$_{100}$, Alm$_{100}$, and Grs$_{100}$, the bulk modulus of Uvr$_{100}$ is smaller. The XRD studies obtained K_{T0} = 157(3)–164(3) GPa, and the BLS and UI study obtained comparable K_{T0} (160.0(20)–163.0(22) GPa).

Therefore, if we only compare the K_{T0} obtained by direct measurements, we have Alm$_{100}$ > Prp$_{100}$ > Grs$_{100}$ > Uvr$_{100}$. As shown in Fig. 4, Alm$_{100}$ is the least compressible and Uvr$_{100}$ is the most compressible. The compression curves of Prp-Cr#0.3, Prp-Cr#4.4, and Prp-Cr#9.3 are very close to that of Grs$_{100}$; Prp-Cr#15.1 is more compressible than Grs$_{100}$, and Prp-Cr#22.4 is only slightly more compressible than Grs$_{100}$ (Fig. 4).

Comparing the volume thermal expansions of the five Cr-pyropes indicates that Prp-Cr#0.3 and Prp-Cr#4.4 have very close thermal expansions, and the expansions of the other three Cr-pyropes are also close (Fig. 5). As shown in Fig. 5, the difference of V_T/V_{T0} between Prp-Cr#0.3 and Prp-Cr#4.4 is less than 0.02% within 296–1000 K; and the difference of V_T/V_{T0} between Prp-Cr#9.3, Prp-Cr#15.1 and Prp-Cr#22.4 is less than 0.03% within 296–1000 K. Prp-Cr#0.3 and Prp-Cr#4.4 expanded more than the other three Cr-pyropes, as shown in Fig. 5, the V_T/V_{T0} of Prp-Cr#4.4 is 0.37% larger than that of Prp-Cr#22.4 at 1000 K.

Several studies Milani et al. (2015, 2017), Skinner (1956) have investigated the thermal expansion behavior of Prp$_{100}$, Alm$_{100}$ and Grs$_{100}$ at room P using XRD (Table S4 and Fig. 5a), which indicates that their thermal expansions have the following relationship: Prp$_{100}$ > Grs$_{100}$ > Alm$_{100}$. As shown in Fig. 5a, the V_T/V_{T0} of Prp$_{100}$ is 0.33% and 0.12% larger than that of Alm$_{100}$ and Grs$_{100}$ at 1000 K, respectively. Currently, no room-P high-T XRD data
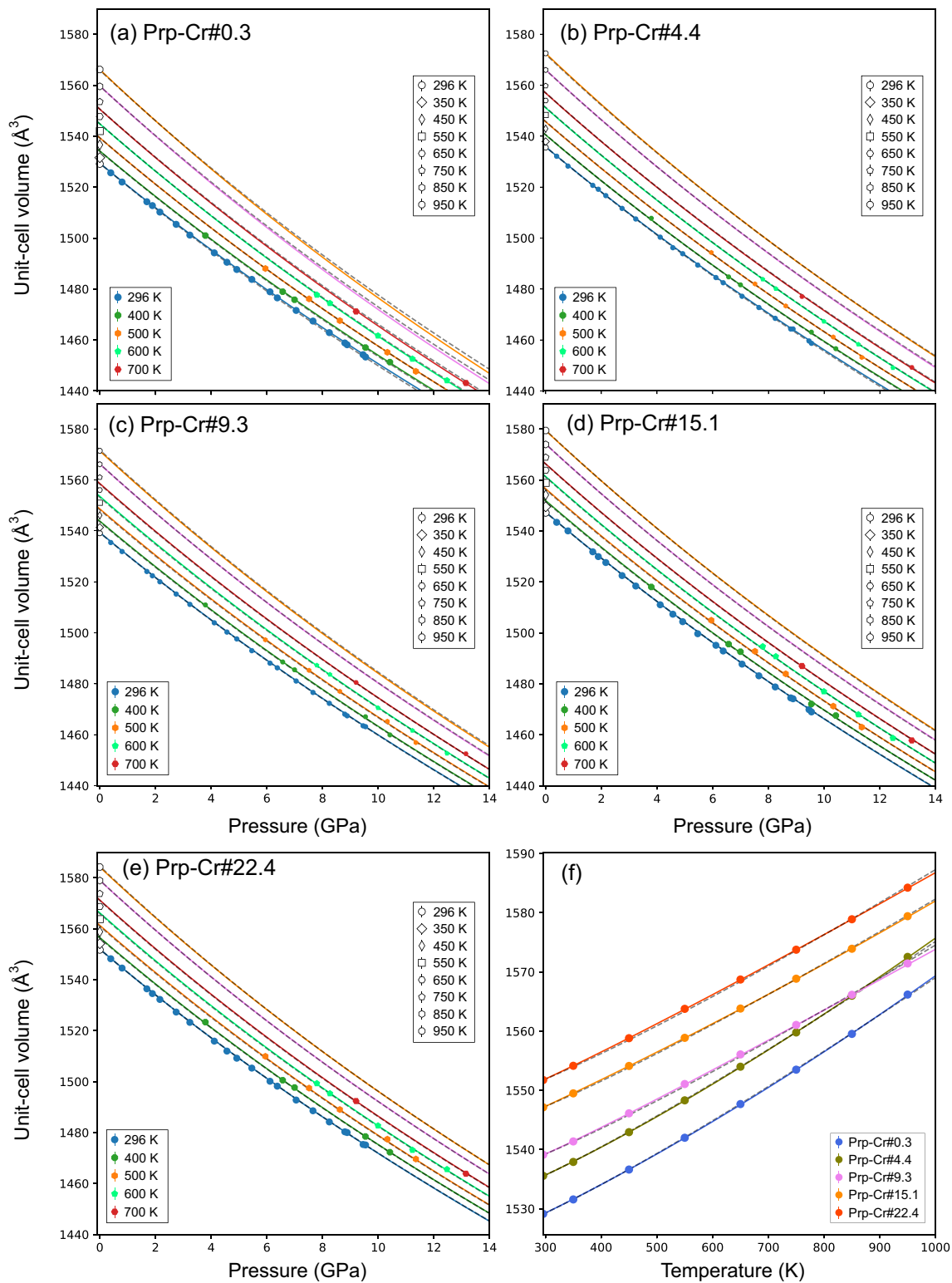
Fig. 3 **a–e** Unit-cell volume for the Cr-pyropes as a function of pressure and temperature. The solid symbols represent data collected at room *T* high *P* and high *P*–*T*, while the open symbols represent data collected at room *P* high *T*. Isothermal curves at 296 K, 400 K, 500 K, 600 K, 700 K, 850 K and 950 K are shown. **f** Unit-cell volume for the Cr-pyropes as a function of temperature and the EoS fitting curves are also shown. In (**a**–**f**), the solid lines are isotherms generated using the BM3 EoS parameters, while the dashed lines are generated using the thermal-pressure EoS parameters. Error bars may be smaller than the symbol size

Table 3 Thermal EoS parameters obtained from the isothermal EoS and thermal-pressure EoS fittings for the Cr-pyropes in this study

	α_{300} ($\times 10^{-5}$ K^{-1})	α_0 (10^{-5} K^{-1})	α_1 (10^{-8} K^{-2})	α_2 (K)	$(\partial K_T/\partial T)_P$ (GPa/K)	δ	θ_E (K)
Prp-Cr#0.3[a]	2.96(13)	2.89(9)	1.41(11)	−0.32(8)	−0.031(4)		
Prp-Cr#0.3[b]	2.96(13)	2.89(9)	1.41(11)	−0.32(8)		5.53(74)	
Prp-Cr#0.3[c]	2.908(3)						522
Prp-Cr#4.4[a]	2.73(15)	3.25(11)	1.04(12)	−0.75(9)	−0.025(4)		
Prp-Cr#4.4[b]	2.72(15)	3.24(10)	1.04(12)	−0.75 (9)		4.58(70)	
Prp-Cr#4.4[c]	2.884(5)						518
Prp-Cr#9.3[a]	2.78(10)	3.41(7)	−0.05(8)	−0.55(6)	−0.022(4)		
Prp-Cr#9.3[b]	2.77(10)	3.40(7)	−0.05(8)	−0.55(6)		4.33(74)	
Prp-Cr#9.3[c]	2.603(5)						515
Prp-Cr#15.1[a]	2.87(10)	2.65(7)	0.83(8)	−0.03(6)	−0.019(3)		
Prp-Cr#15.1[b]	2.85(10)	2.65(7)	0.83(8)	−0.04(6)		3.83(68)	
Prp-Cr#15.1[c]	2.568(4)						512
Prp-Cr#22.4[a]	2.75(10)	3.21(7)	0.17(8)	−0.46(6)	−0.023(3)		
Prp-Cr#22.4[a]	2.76(8)	3.22(6)	0.17(8)	−0.46(5)		4.64(61)	
Prp-Cr#22.4[b]	2.569(5)						508

[a]Isothermal BM3 EoS with $(\partial K_T/\partial T)_P$

[b]Isothermal BM3 EoS with δ

[c]Holland and Powell (2011) thermal-pressure EoS
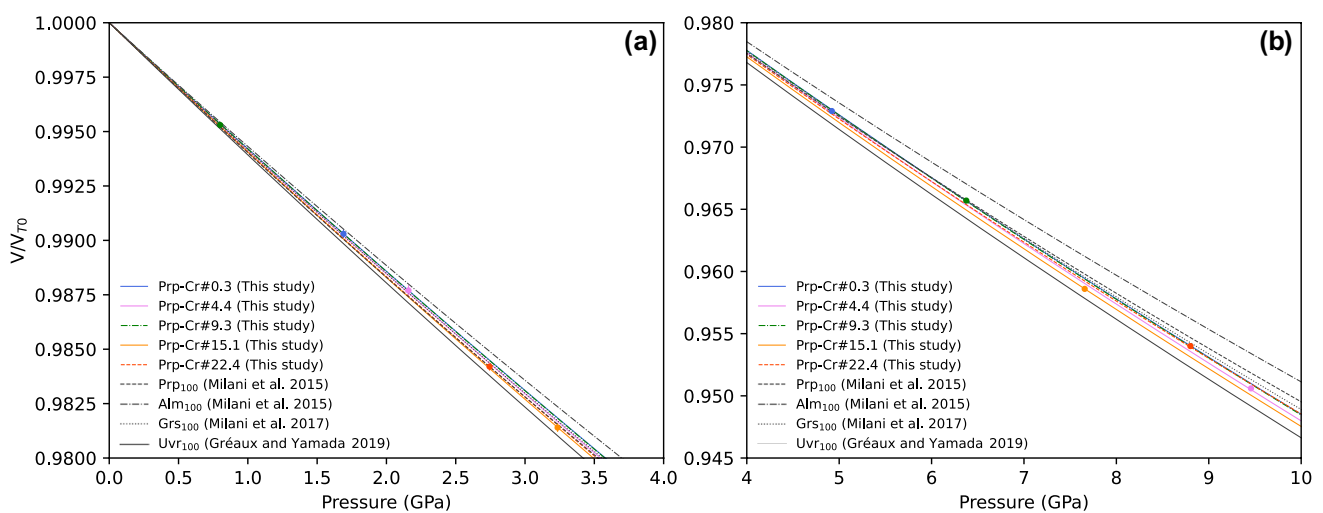
Fig. 4 V/V_{T0} as a function of pressure for the Cr-pyropes and end-member Prp$_{100}$, Alm$_{100}$, Grs$_{100}$ and Uvr$_{100}$. **a** 0–4 GPa; **b** 4–10 GPa. The data of the end-member garnets are from previous studies Gré-aux and Yamada (2019), Milani et al. (2015, 2017), while the data of the Cr-pyropes are from this study. Error bars may be smaller than the symbol size

are available for Uvr$_{100}$, but Gréaux and Yamada (2019) reported the thermal expansivity of Uvr$_{100}$ based on their high *P–T* XRD data, indicating that the thermal expansion of Uvr$_{100}$ is higher than that of Alm$_{100}$ but lower than that of Prp$_{100}$ and Grs$_{100}$ (Fig. 5a). In comparison with the end-member garnets, the five Cr-pyropes have larger expansivities. For instance, at 1000 K, the V_T/V_{T0} of Prp-Cr#0.3 is 0.58% larger than that of Prp$_{100}$, and the V_T/V_{T0} of Prp-Cr#15.1 is 0.20% larger than that of Prp$_{100}$ (Fig. 5a).

The α_{300} of the five Cr-pyropes are close within the uncertainty. As shown in Table 3 and Fig. 6a, the α_{300} of the five Cr-pyropes are 2.73(15)–2.96(13) $\times 10^{-5}$ K^{-1}. These values of α_{300} are comparable to the α_{300} of Prp$_{100}$ reported by Milani et al. (2015) and Skinner (1956) within the uncertainty but are larger than that reported by Thieblot et al. (1998) (Fig. 6 and Table S4). In comparison with these Cr-pyropes, Alm$_{100}$ has a lower value of α_{300} (Skinner 1956); the α_{300} of Grs$_{100}$ reported by Milani et al. (2017), Skinner
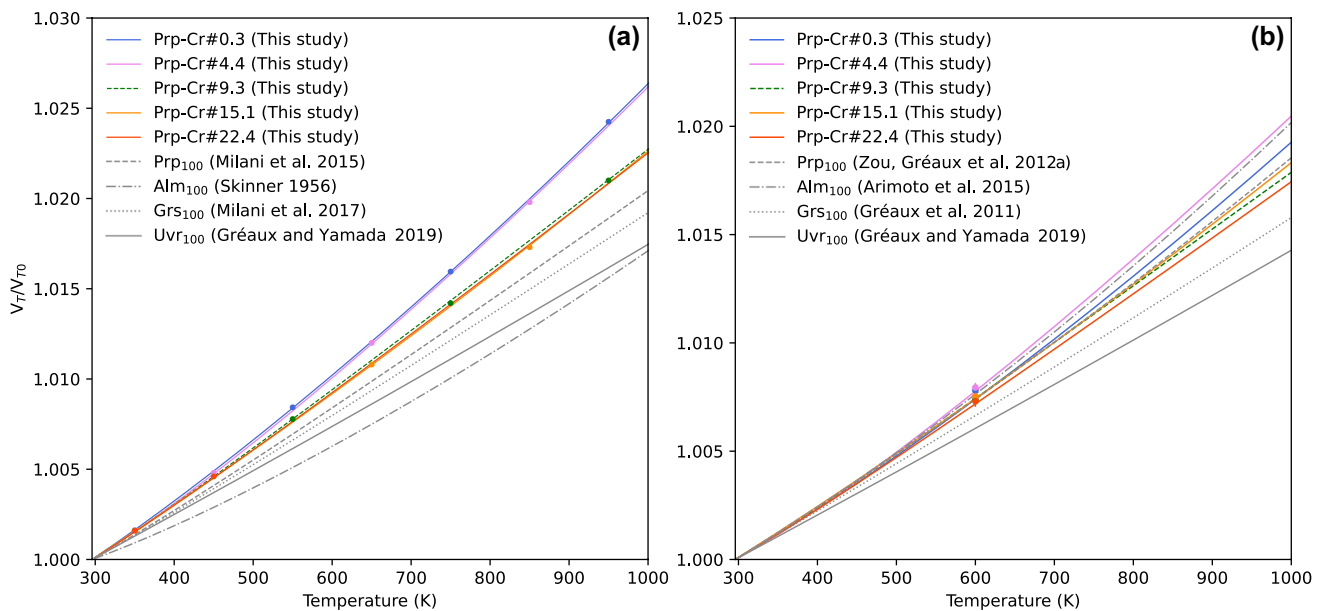
Fig. 5 V_T/V_{T0} as a function of temperature for the Cr-pyropes and Prp$_{100}$, Alm$_{100}$, Grs$_{100}$ and Uvr$_{100}$ at room P (**a**) and 10 GPa (**b**). The data of the Cr-pyropes are from this study, while the data of the end-member garnets are from previous studies Arimoto et al. (2015), Gré-

aux et al. (2011), Gréaux and Yamada (2019), Milani et al. (2015, 2017), Skinner (1956), Zou et al. (2012a). Error bars may be smaller than the symbol size
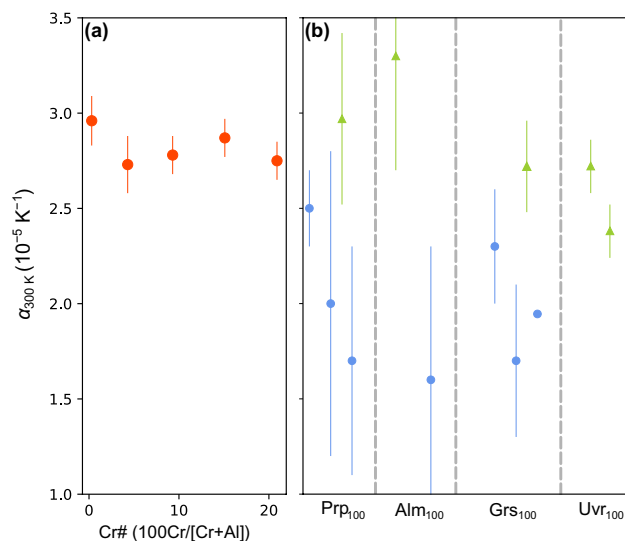

Fig. 6 Thermal expansion coefficients at 300 K (α_{300}) for Cr-pyropes (**a**) in this study and end-member (**b**) pyrope, almandine, grossular and uvarovite from previous studies. Light blue balls represent results obtained from room-P high-T XRD studies Milani et al. (2015, 2017), Skinner (1956), Thieblot et al. (1998) while light green triangles represent results obtained from high P–T XRD studies Arimoto et al. (2015), Fan et al. (2015), Gréaux et al. (2011), Gréaux and Yamada (2019), Zou et al. (2012a)

(1956) and Thieblot et al. (1998) are smaller than the α_{300} of the Cr-pyropes (Fig. 6 and Table S4). Gréaux and Yamada (2019) reported for Uvr$_{100}$ $\alpha_{300} = 2.37(20) \times 10^{-5}$ K^{-1} which

was smaller than that of Cr-pyropes in this study while Fan et al. (2015) reported an α_{300} (2.72(14) $\times 10^{-5}$ K^{-1}) that was comparable to that of the Cr-pyropes.

We also compared our high P–T data with previous studies to determine if the Cr-pyropes have higher thermal expansivities than the end-member garnets at high P. We selected Prp-Cr#9.3 and compared its high P–T data with those of Prp$_{100}$ (Zou et al. 2012a), Alm$_{100}$ (Arimoto et al. 2015), Grs$_{100}$ (Gréaux et al. 2011) and Uvr$_{100}$ (Gréaux and Yamada 2019). As shown in Fig. 7a, b, at high P, Prp$_{100}$ and Prp-Cr#9.3 have very close thermal expansivities; Alm$_{100}$ has distinctively higher thermal expansivity than Prp-Cr#9.3, while the thermal expansivity of the latter is observably higher than that of Grs$_{100}$ and Uvr$_{100}$ (Fig. 7c, d). To make the comparisons straightforward and include the other four Cr-pyropes, we compared the V_T/V_{T0} of the Cr-pyropes and end-member garnets as a function of temperature at 10 GPa (Fig. 5b). As shown in Fig. 5b, when $T < 550$ K, the Cr-pyropes, Prp$_{100}$, and Alm$_{100}$ have very close thermal expansivities, the differences in V_T/V_{T0} are below 0.02%. However, the differences increase with increasing temperature. Alm$_{100}$ has distinctively higher thermal expansivity than Prp$_{100}$ at $T > 550$ K, as shown in Fig. 5b, the V_T/V_{T0} of the former is 0.16% higher than that of the latter at 1000 K. For the Cr-pyropes, the thermal expansivity of Prp-Cr#0.3 is between that of Prp$_{100}$ and Alm$_{100}$, and the V_T/V_{T0} of Prp-Cr#0.3 is 0.07% higher than that of Prp$_{100}$ but 0.09% lower than that of Alm$_{100}$ at 1000 K; the V_T/V_{T0} of Prp-Cr#4.4 is 0.03% higher than that of Alm$_{100}$ at 1000 K; the thermal

Fig. 7 **a**–**d** the normalized unit-cell volume of Prp-Cr#9.3 as a function of pressure and temperature in comparison with the end-ember Prp$_{100}$ (**a**), Alm$_{100}$ (**b**), Grs$_{100}$ (**c**) and Uvr$_{100}$ (**d**); **e**–**h** unit-cell volume of Cr-pyropes Prp-Cr#0.3 (**e**), Prp-Cr#4.4 (**f**), Prp-Cr#9.3 (**g**), Prp-Cr#15.1 (**h**) as a function of pressure and temperature in comparison with end-member mixing unit-cell volume. The solid symbols represent data of the Cr-pyropes collected at room *T* high *P* and high *P*–*T*, while the open symbols represent that collected at room *P* high *T*. Isothermal curves at 296 K, 400 K, 500 K, 600 K, 700 K, 850 K and 950 K are shown. Solid curves are generated using the EoS parameters of the Cr-pyropes. The dashed curves in (**a-d**) are generated using the EoS parameters of the end-member garnets from previous studies Arimoto et al. (2015), Gréaux et al. (2011), Gréaux and Yamada (2019), Zou et al. (2012a). In (**e–h**), the dotted curves represent end-member mixing unit-cell volumes, while dashed curves represent the corrected end-member mixing unit-cell volumes. Error bars may be smaller than the symbol size
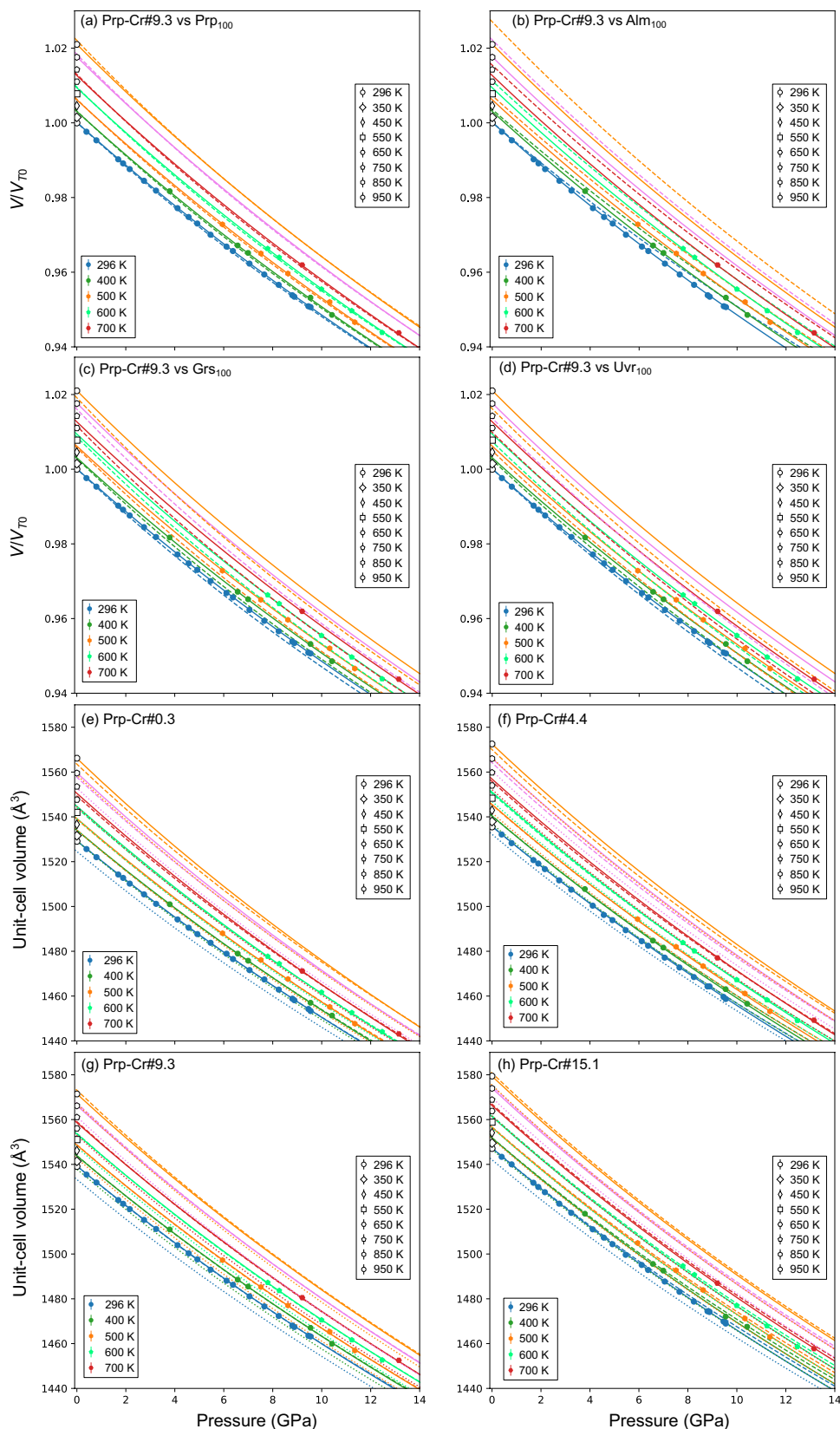
expansivities of the other three Cr-pyropes are lower than that of Prp_{100}, as shown in Fig. 5b, at 1000 K, the V_T/V_{T0} of Prp_{100} is 0.07%, 0.02%, and 0.11% higher than that of Prp-Cr#9.3, Prp-Cr#15.1 and Prp-Cr#22.4, respectively. By comparison, Grs_{100} and Uvr_{100} have distinctively lower thermal expansivities than Prp100, Alm100, and the Cr-pyropes. As shown in Fig. 5b, at 1000 K, the V_T/V_{T0} of Grs_{100} and Uvr_{100} are 0.16% and 0.31% lower than that of Prp-Cr#22.4, respectively. Therefore, at high P, the thermal expansivities of Prp-Cr#0.3 and Prp-Cr#4.4 are higher than that of Prp_{100}, while the other three Cr-pyropes have lower thermal expansivities than Prp_{100}.

To determine if the EoS of the Cr-pyropes predicts significant larger volumes than the mix (Vegard's law) of the end-member volumes at high $P–T$, we compared the high $P–T$ data and the EoS of the Cr-pyropes with the end-member mixing volumes derived from established EoS based on high $P–T$ data. We adopted EoS parameters (Tables S3–S5) of Prp_{100} (Zou et al. 2012b), Alm_{100} (Arimoto et al. 2015), Grs_{100} (Gréaux et al. 2011), Adr_{100} (Pavese et al. 2001a), Sps_{100} (Gréaux and Yamada 2014), and Uvr_{100} (Gréaux and Yamada 2019) to calculate the end-member volumes at high $P–T$, and then we calculated the corresponding end-member mixing volumes according to the compositions of Cr-pyropes (Table 1). We did not include other end members (e.g., schorlomite-Al, skiagite) into the calculation as they are very minor components in the Cr-pyrope. We did not include Prp-Cr#22.4 in the comparison, as it contains 5.0 mol. % Knr_{100} and the EoS parameters are currently unavailable for pure Knr_{100}. The results are shown in Fig. 7e–h, indicating that the EoS of the Cr-pyrope predicts larger volumes than the end-member mixing models, as the V_{T0} of the former are larger than that of the latter (Table S6). After the discrepancy in V_{T0} is corrected, the EoS of Cr-pyrope predicts much more consistent values with the end-member mixing model. As shown in Fig. 7e–f, the EoS of Prp-Cr#0.3 and Prp-Cr#4.4 predict consistent volumes with the end-member mixing model at $T < 700$ K, and the discrepancies increase with increasing temperature while decrease with increasing pressure. For instance, at 950 K the EoS of Prp-Cr#0.3 predicts 0.16% and 0.05% higher volumes than the end-member mixing model at 0 GPa and 10 GPa, respectively. By comparison, the EoS of Prp-Cr#9.3 predicts consistent volumes with the end-member mixing model at high $P–T$, and the maximum difference is 0.1% within the $P–T$ range (Fig. 7g); the EoS of Prp-Cr#15.1 predicts smaller volumes than that of the end-member mixing model, as shown in Fig. 7h, the former are 0.07–0.09% smaller than the latter at 950 K.

Previous room-P high-T XRD studies Milani et al. (2015, 2017), Skinner (1956); Thieblot et al. (1998) reported much lower thermal expansivities for Prp_{100}, Alm_{100}, and Grs_{100} (Tables S4–S7), in comparison with the results reported by

the high $P–T$ XRD studies Arimoto et al. (2015), Gréaux et al. (2011), Zou et al. (2012a). In this study, the thermal expansivities of the Cr-pyropes are higher than the end-member garnets (Prp_{100}, Alm_{100}, and Grs_{100}) when compared with the room-P high-T data from previous studies (Fig. 5a). However, the thermal expansivities of the Cr-pyropes are comparable to that of Prp_{100} and Alm_{100}, although they are higher than that of Grs_{100} and Uvr_{100} when compared with the high $P–T$ data from previous studies (Figs. 5b). Therefore, the higher thermal expansivities of the five Cr-pyropes in comparison with the results from previous room-P high-T XRD studies do not necessarily indicate high excess thermal expansivity in Cr-pyropes. Moreover, the EoS of the Cr-pyropes predicts comparable volumes to that of the end-member mixing models (Fig. 7(e–h)), and the maximum discrepancy is ~ 0.2% which is small considering the uncertainties of thermal expansivity (~ 10%; Table S4), although the larger V_{T0} in comparison with the end-member mixing model indicate positive excess volume (0.2–0.4%; Table S6). Therefore, the excess thermal expansivity in Cr-pyrope, if any, should be rather small.

The $(\partial K_T/\partial T)_P$ of the five Cr-pyropes are within $-0.031(4)$ to $-0.019(3)$ GPa/K. As shown in Fig. 8 and Table 3, Prp-Cr#0.3 has distinctly smaller $(\partial K_T/\partial T)_P$ ($-0.031(4)$ GPa/K) than the others, while the other four Cr-pyropes have close values of $(\partial K_T/\partial T)_P$ ($-0.025(4)$ to $-0.019(3)$ GPa/K). Few studies reported the $(\partial K_T/\partial T)_P$ of end-member garnets (Arimoto et al. 2015; Fan et al. 2019; Gréaux et al. 2011;
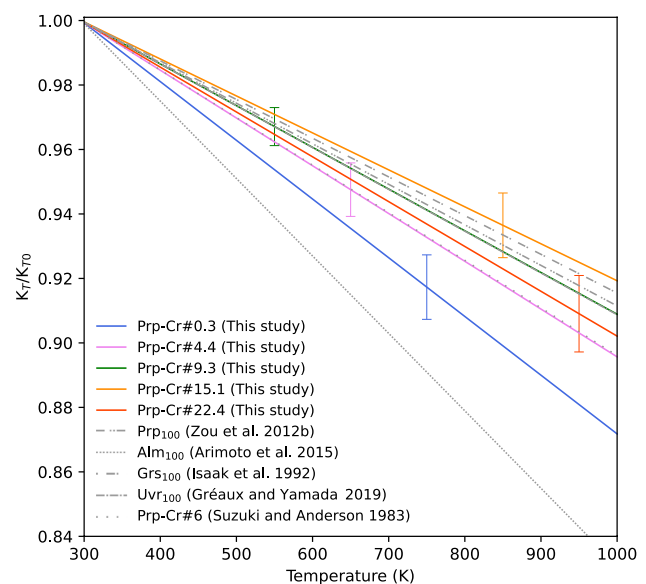

Fig. 8 K_T/K_{T0} as a function of temperature for the Cr-pyropes and Prp_{100}, Alm_{100}, Grs_{100} and Uvr_{100}. The data of the end-member garnets and one of the Cr-pyropes (Prp-Cr#6) are from previous studies Arimoto et al. (2015), Gréaux and Yamada (2019), Isaak et al. (1992), Suzuki and Anderson (1983), Zou et al. (2012b), while the data of the other Cr-pyropes are from this study

Gréaux and Yamada 2019; Isaak et al. 1992; Sinogeikin and Bass 2000; Zou et al. 2012a, b), and their results revealed that Prp_{100}, Grs_{100}, and Uvr_{100} have very close values of $(\partial K_T/\partial T)_P$ ($-0.021(1)$ to $-0.017(2)$ GPa/K; Fig. 8 and Table S5), while Alm_{100} has a significantly lower $(\partial K_T/\partial T)_P$ ($-0.043(14)$ GPa/K). Thus, for the five Cr-pyropes, the $(\partial K_T/\partial T)_P$ of Prp-Cr#4.4, Prp-Cr#9.3, Prp-Cr#15.1, and Prp-Cr#22.4 are close to the trend of Prp_{100}, Grs_{100}, and Uvr_{100}, while Prp-Cr#0.3 is closer to the Alm_{100} trend (Fig. 8) than the other four Cr-pyropes. Moreover, utilizing RPR, Suzuki and Anderson (1983) measured the high-T elasticity of a natural Cr-pyrope (Prp-Cr#6) whose chemical composition was close to the Prp-Cr#4.4 in this study, and they obtained a close value of $(\partial K_T/\partial T)_P$ ($-0.025(1)$ GPa/K; Fig. 8 and Table S5), indicating that the EoS fitting of this study yielded comparable values of $(\partial K_T/\partial T)_P$ to that obtained by direct measurement of elasticity.

To summarize, the results of this study indicate that (a) the Cr-pyropes have K_{T0} very close to Prp_{100} and the difference is less than 3% within the composition range in this study, (b) the Cr-pyropes have larger thermal expansivities than the end-member garnets when compared with the room-P high-T XRD results, but they are comparable when compared with the high P–T XRD results, and (c) the $(\partial K_T/\partial T)_P$ of the Cr-pyropes are close to that of the end-member Prp_{100}, Grs_{100}, and Uvr_{100} but are distinctively larger than that of Alm_{100}.

Application to calculating entrapment pressure of garnet in peridotitic diamond

Garnet inclusions in peridotitic diamond are Cr-pyropes (Stachel and Harris 2008). Therefore, our results on the thermal EoS of Cr-pyropes are applicable to calculating the entrapment pressure (P_e) of peridotitic diamonds that have garnet inclusions using the diamond–garnet geo-barometry. The results of this study also indicate the compositional effects on the thermal EoS parameters of Cr-pyropes. It is, therefore, necessary to investigate the compositional effects on calculated P_e. Therefore, we calculate P_e of the Cr-pyropes in this study and end-member garnets as inclusions in diamond, and we analyze the calculated results to evaluate the compositional effects on calculated P_e.

The use of diamond–garnet geo-barometry to calculate P_e is based on the elasticity theory and several assumptions, which have been described in great detail by several studies (e.g., Angel et al. 2014a, 2017; Milani et al. 2015). The diamond–garnet geo-barometry uses the residual pressure (P_i) exerted by the host (diamond) on the inclusion (garnet) and the thermal EoS parameters of both the inclusion and host to generate an isomeke which represents possible entrapment $P(P_e)$ – T conditions. Here, to calculate P_e, we

assume $P_i = 0.2$ GPa which could be for garnet inclusion in peridotitic diamond (Izraeli et al. 1999). Using the EosFit-Pinc software (Angel et al. 2017), we calculate P_e for the five Cr-pyropes in this study using the obtained thermal EoS parameters (Tables 2, 3). In the calculation, the BM3 EoS is used, and the used thermal EoS parameters of diamond are from Angel et al. (2015). Using the same method and the thermal EoS parameters summarized in Table S7 (Arimoto et al. 2015; Gréaux et al. 2011; Gréaux and Yamada 2019; Isaak et al. 1992; Milani et al. 2015, 2017; Sinogeikin and Bass 2000; Skinner 1956; Zou et al. 2012a), the P_e of Prp_{100}, Alm_{100}, Grs_{100}, and Uvr_{100} are also calculated. The uncertainty of the calculated P_e is estimated from the uncertainties of the measured thermal EoS parameters.

The results indicate that the discrepancy in thermal expansivity largely influences the P_e of Cr-pyrope. As shown in Fig. 9 and Table S8, the P_e of Prp-Cr#0.3 and Prp-Cr#4.4 are close to each other, and Prp-Cr#9.3, Prp-Cr#15.1 and Prp-Cr#22.4 have very close P_e, which is very consistent with the differences in their thermal expansion behavior, namely, Prp-Cr#0.3 and Prp-Cr#4.4 have comparable expansivities, while Prp-Cr#9.3, Prp-Cr#15.1 and Prp-Cr#22.4 are also very close in thermal expansion behavior (Fig. 5a). Therefore, for the Cr-pyropes, the variation in thermal expansion behavior plays a more significant role in influencing the calculated P_e in comparison with the compressional behavior. As shown in Table 2, the K_{T0} of the five Cr-pyropes are very
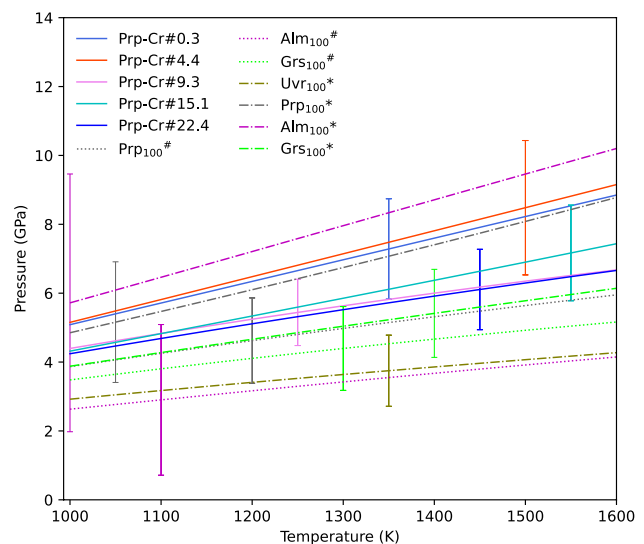
Fig. 9 Calculated entrapment pressure (P_e) as a function of temperature for the Cr-pyropes and end-member garnets (Prp_{100}, Alm_{100}, Grs_{100} and Uvr_{100}) in diamond assuming a residual pressure of $P_i = 0.2$ GPa. Solid curves represent Cr-pyrope P_e, dash-dotted and dotted curves represent P_e of end-member garnets calculated using thermal expansivities obtained from high P–T XRD and room-P high-T XRD, respectively. An error bar is shown for each curve. Data of this figure are also shown in Tables S8–9

close to each other (K_{T0} = 165.4(37)–170.2(35) GPa), and the difference is up to 2.8% which is much smaller than the difference in the thermal expansivity (up to 8.8%).

Likewise, the discrepancies between the room-P high-T and high P–T XRD studies in the thermal expansivities of end-member garnets lead to very different P_e. As shown in Fig. 9 and Table S9, using the thermal expansivities obtained by the room-P high-T XRD studies yield distinctively lower P_e for Prp_{100}, Alm_{100}, and Grs_{100} than using the thermal expansivities obtained by the high P–T XRD studies. The calculated P_e of Cr-pyropes are more consistent with the end-member P_e calculated using the thermal expansivities obtained by the high P–T XRD than by the room-P high-T XRD. As shown in Fig. 9, Prp-Cr#0.3 and Prp-Cr#4.4 have very close P_e to Prp_{100}, while the P_e of Prp-Cr#9.3, Prp-Cr#15.1, and Prp-Cr#22.4 are much closer to Grs_{100} and Uvr_{100} (Fig. 9).

Supplementary Information The online version contains supplementary material available at https://doi.org/10.1007/s00410-022-01932-7.

References

Angel RJ (2000) Equations of state rev. Mineral Geochem 41(1):35–59. https://doi.org/10.2138/rmg.2000.41.2

Angel RJ, Mazzucchelli ML, Alvaro M, Nimis P, Nestola F (2014a) Geobarometry from host-inclusion systems: the role of elastic relaxation. Am Mineral 99(10):2146–2149. https://doi.org/10.2138/am-2014-5047

Angel RJ, Gonzalez-Platas J, Alvaro M (2014b) EosFit7c and a Fortran module (library) for equation of state calculations. Z Krystallogr 229(5):405–419. https://doi.org/10.1515/zkri-2013-1711

Angel RJ, Alvaro M, Nestola F, Mazzucchelli ML (2015) Diamond thermoelastic properties and implications for determining the pressure of formation of diamond-inclusion systems. Russ Geol Geophys 56(1):211–220. https://doi.org/10.1016/j.rgg.2015.01.014

Angel RJ, Mazzucchelli ML, Alvaro M, Nestola F (2017) EosFit-Pinc: A simple GUI for host-inclusion elastic thermobarometry. Am Mineral 102:1957–1960. https://doi.org/10.2138/am-2017-6190

Arimoto T, Gréaux S, Irifune T, Zhou C, Higo Y (2015) Sound velocities of $Fe_3Al_2Si_3O_{12}$ almandine up to 19 GPa and 1700 K. Phys Earth Planet 246:1–8. https://doi.org/10.1016/j.pepi.2015.06.004

Babuška V, Fiala J, Kumazawa M, Ohno I, Sumino Y (1978) Elastic properties of garnet solid-solution series. Phys Earth Planet 16(2):157–176. https://doi.org/10.1016/0031-9201(78)90086-9

Banas A, Stachel T, Muehlenbachs K, McCandless TE (2007) Diamonds from the Buffalo Head Hills, Alberta: formation in a nonconventional setting. Lithos 93(1):199–213. https://doi.org/10.1016/j.lithos.2006.07.001

Banas A, Stachel T, Phillips D, Shimizu N, Viljoen KS, Harris JW (2009) Ancient metasomatism recorded by ultra-depleted garnet inclusions in diamonds from DeBeers Pool South Africa. Lithos 112(Supplement 2):736–746. https://doi.org/10.1016/j.lithos.2009.04.043

Bass JD (1986) Elasticity of uvarovite and andradite garnets. J Geophys Res 91(B7):7505–7516. https://doi.org/10.1029/JB091iB07p07505

Bass JD (1989) Elasticity of grossular and spessartite garnets by Brillouin spectroscopy. J Geophys Res 94(B6):7621–7628. https://doi.org/10.1029/JB094iB06p07621

Beyer C, Kurnosov AV, Ballaran TB, Frost DJ (2021) High-pressure and high-temperature single-crystal X-ray diffraction of complex garnet solid solutions up to 16 GPa and 823 K. Phys Chem Miner 48(4):17. https://doi.org/10.1007/s00269-021-01139-5

Birch F (1947) Finite elastic strain of cubic crystals. Phys Rev 71(11):809–824. https://doi.org/10.1103/PhysRev.71.809

Chai M, Brown JM, Slutsky LJ (1997) The elastic constants of a pyrope-grossular-almandine garnet to 20 Gpa. Geophys Res Lett 24(5):523–526. https://doi.org/10.1029/97GL00371

Chantel J, Manthilake GM, Frost DJ, Beyer C, Ballaran TB, Jing Z, Wang Y (2016) Elastic wave velocities in polycrystalline $Mg_3Al_2Si_3O_{12}$-pyrope garnet to 24 GPa and 1300 K. Am Mineral 101(4):991–997. https://doi.org/10.2138/am-2016-5335

Chen G, Cooke JA, Gwanmesia GD, Liebermann RC (1999) Elastic wave velocities of $Mg_3Al_2Si_3O_{12}$-pyrope garnet to 10 GPa. Am Mineral 84(3):384–388. https://doi.org/10.2138/am-1999-0322

Chi J (1996) Kimberlite and paleozoic lithospheric mantle characteristics of North China Platform. Science Press, Beijing

Conrad PG, Zha C-S, Mao H-K, Hemley RJ (1999) The high-pressure, single-crystal elasticity of pyrope, grossular, and andradite. Am Mineral 84(3):374–383. https://doi.org/10.2138/am-1999-0321

Davies RM, Griffin WL, O'Reilly SY, Doyle BJ (2004a) Mineral inclusions and geochemical characteristics of microdiamonds from the DO27, A154, A21, A418, DO18, DD17 and Ranch Lake kimberlites at Lac de Gras, Slave Craton, Canada. Lithos 77(1):39–55. https://doi.org/10.1016/j.lithos.2004.04.016

Davies RM, Griffin WL, O'Reilly SY, McCandless TE (2004b) Inclusions in diamonds from the K14 and K10 kimberlites, Buffalo Hills, Alberta, Canada: diamond growth in a plume? Lithos 77(1):99–111

Deines P, Harris JW (2004) New insights into the occurrence of 13C-depleted carbon in the mantle from two closely associated kimberlites: Letlhakane and Orapa, Botswana. Lithos 77(1):125–142. https://doi.org/10.1016/j.lithos.2004.04.015

Deines P, Harris JW, Gurney JJ (1991) The carbon isotopic composition and nitrogen content of lithospheric and asthenospheric diamonds from the Jagersfontein and Koffiefontein kimberlite, South Africa. Geochim Cosmochim Acta 55(9):2615–2625. https://doi.org/10.1016/0016-7037(91)90377-H

Dera P, Zhuravlev K, Prakapenka V, Rivers ML, Finkelstein GJ, Grubor-Urosevic O, Tschauner O, Clark SM, Downs RT (2013) High pressure single-crystal micro X-ray diffraction analysis with GSE_ADA/RSV software. High Press Res 33(5):466–484. https://doi.org/10.1080/08957959.2013.806504

Dewaele A, Datchi F, Loubeyre P, Mezouar M (2008) High pressure–high temperature equations of state of neon and diamond. Phys Rev B 77(9):094106. https://doi.org/10.1103/PhysRevB.77.094106

Diella V, Sani A, Levy D, Pavese A (2004) High-pressure synchrotron X-ray diffraction study of spessartine and uvarovite: a comparison between different equation of state models. Am Mineral 89(2–3):371–376. https://doi.org/10.2138/am-2004-2-317

Donnelly CL, Stachel T, Creighton S, Muehlenbachs K, Whiteford S (2007) Diamonds and their mineral inclusions from the A154 South pipe, Diavik Diamond Mine, Northwest territories, Canada. Lithos 98(1):160–176. https://doi.org/10.1016/j.lithos.2007.03.003

Dorogokupets P, Dewaele A (2007) Equations of state of MgO, Au, Pt, NaCl-B1, and NaCl-B2: Internally consistent high-temperature pressure scales. High Press Res 27(4):431–446. https://doi.org/10.1080/08957950701659700

Du W, Clark SM, Walker D (2015) Thermo-compression of pyrope-grossular garnet solid solutions: Non-linear compositional dependence. Am Mineral 100(1):215–222. https://doi.org/10.2138/am-2015-4752

Dymshits AM, Litasov KD, Sharygin IS, Shatskiy A, Ohtani E, Suzuki A, Funakoshi K (2014) Thermal equation of state of majoritic knorringite and its significance for continental upper mantle. J Geophys Res 119(11):8034–8046. https://doi.org/10.1002/2014JB011194

Fan D, Xu J, Ma M, Wei S, Zhang B, Liu J, Xie H (2015) *P-V-T* equation of state of $Ca_3Cr_2Si_3O_{12}$ uvarovite garnet by using a diamond-anvil cell and in-situ synchrotron X-ray diffraction. Am Mineral 100(2–3):588–597. https://doi.org/10.2138/am-2015-5002

Fan D, Kuang Y, Xu J, Li B, Zhou W, Xie H (2017) Thermoelastic properties of grossular–andradite solid solution at high pressures and temperatures. Phys Chem Miner 44(2):137–147. https://doi.org/10.1007/s00269-016-0843-4

Fan D, Xu J, Lu C, Tkachev SN, Li B, Ye Z, Huang S, Prakapenka VB, Zhou W (2019) Elasticity of single-crystal low water content hydrous pyrope at high-pressure and high-temperature conditions. Am Mineral 104(7):1022–1031. https://doi.org/10.2138/am-2019-6897

Fei Y (1995) Thermal expansion. In: Ahrens TJ (ed) Mineral physics and crystallography: a handbook of physical constants. American Geophysical Union, Washington DC, pp 29–44

Freund J, Ingalls R (1989) Inverted isothermal equations of state and determination of B_0, B'_0 and B_0. J Phys Chem Soli 50(3):263–268. https://doi.org/10.1016/0022-3697(89)90486-1

Geiger CA (2008) Silicate garnet: A micro to macroscopic (re)view. Am Mineral 93(2–3):360–372. https://doi.org/10.2138/am.2008.2588

Gilio M, Angel RJ, Alvaro M (2021) Elastic geobarometry: How to work with residual inclusion strains and pressures. Am Mineral 106(9):1530–1533. https://doi.org/10.2138/am-2021-7928

Gillet P, Fiquet G, Daniel I, Reynard B, Hanfland M (1999) Equations of state of ^{12}C and ^{13}C diamond. Phys Rev B 60(21):14660–14664. https://doi.org/10.1103/PhysRevB.60.14660

Gonzalez-Platas J, Alvaro M, Nestola F, Angel R (2016) EosFit7-GUI: a new graphical user interface for equation of state calculations, analyses and teaching. J Appl Crystallogr 49(4):1377–1382. https://doi.org/10.1107/s1600576716008050

Gréaux S, Yamada A (2014) *P-V-T* equation of state of $Mn_3Al_2Si_3O_{12}$ spessartine garnet. Phys Chem Miner 41(2):141–149. https://doi.org/10.1007/s00269-013-0632-2

Gréaux S, Yamada A (2019) Density variations of Cr-rich garnets in the upper mantle inferred from the elasticity of uvarovite garnet. C R Geosci 351(2):95–103. https://doi.org/10.1016/j.crte.2018.09.012

Gréaux S, Kono Y, Nishiyama N, Kunimoto T, Wada K, Irifune T (2011) *P-V-T* equation of state of $Ca_3Al_2Si_3O_{12}$ grossular garnet. Phys Chem Miner 38(2):85–94. https://doi.org/10.1007/s00269-010-0384-1

Grew ES, Locock AJ, Mills SJ, Galuskina IO, Galuskin EV, Hålenius U (2013) Nomenclature of the garnet supergroup. Am Mineral 98(4):785–811. https://doi.org/10.2138/am.2013.4201

Griffin WL, Sobolev NV, Ryan CG, Pokhilenko NP, Win TT, Yefimova ES (1993) Trace elements in garnets and chromites: diamond formation in the Siberian lithosphere. Lithos 29(3):235–256. https://doi.org/10.1016/0024-4937(93)90019-9

Griffin WL, Win TT, Davies R, Wathanakul P, Andrew A, Metcalfe I, Cartigny P (2001) Diamonds from Myanmar and Thailand: characteristics and possible origins. Econ Geol 96(1):0159–0170

Gwanmesia GD, Zhang J, Darling K, Kung J, Li B, Wang L, Neuville D, Liebermann RC (2006) Elasticity of polycrystalline pyrope ($Mg_3Al_2Si_3O_{12}$) to 9 GPa and 1000 °C. Phys Earth Planet 155(3):179–190. https://doi.org/10.1016/j.pepi.2005.10.008

Gwanmesia G, Jackson I, Liebermann R (2007) In search of the mixed derivative $\partial^2 M/\partial P\partial T$ (M= G, K): joint analysis of ultrasonic data for polycrystalline pyrope from gas-and solid-medium apparatus. Phys Chem Miner 34(2):85–93

Gwanmesia GD, Wang L, Heady A, Liebermann RC (2014) Elasticity and sound velocities of polycrystalline grossular garnet ($Ca_3Al_2Si_3O_{12}$) at simultaneous high pressures and high temperatures. Phys Earth Planet 228:80–87. https://doi.org/10.1016/j.pepi.2013.09.010

Harris JW, Stachel T, Léost I, Brey GP (2004) Peridotitic diamonds from Namibia: constraints on the composition and evolution of their mantle source. Lithos 77(1):209–223. https://doi.org/10.1016/j.lithos.2004.03.028

Hazen RM, Finger LW (1978) Crystal structures and compressibilities of pyrope and grossular to 60 kbar. Am Mineral 63(3–4):297–303

Helffrich G, Connolly JAD (2009) Physical contradictions and remedies using simple polythermal equations of state. Am Mineral 94(11–12):1616–1619. https://doi.org/10.2138/am.2009.3262

Holland T, Powell R (2011) An improved and extended internally consistent thermodynamic dataset for phases of petrological interest, involving a new equation of state for solids. J Metamorph Geol 29(3):333–383. https://doi.org/10.1111/j.1525-1314.2010.00923.x

Huang S, Chen JH (2014) Equation of state of pyrope-almandine solid solution measured using a diamond anvil cell and in situ synchrotron X-ray diffraction. Phys Earth Planet 228:88–91. https://doi.org/10.1016/j.pepi.2014.01.014

Hunt L, Stachel T, McCandless TE, Armstrong J, Muelenbachs K (2012) Diamonds and their mineral inclusions from the Renard kimberlites in Quebec. Lithos 142–143(Supplement C):267–284. https://doi.org/10.1016/j.lithos.2012.02.022

Isaak DG, Anderson OL, Oda H (1992) High-temperature thermal expansion and elasticity of calcium-rich garnets. Phys Chem Miner 19(2):106–120. https://doi.org/10.1007/BF00198608

Ita J, Stixrude L (1992) Petrology, elasticity, and composition of the mantle transition zone. J Geophys Res 97(B5):6849–6866. https://doi.org/10.1029/92JB00068

Izraeli E, Harris J, Navon O (1999) Raman barometry of diamond formation. Earth Planet Sci Lett 173(3):351–360. https://doi.org/10.1016/S0012-821X(99)00235-6

Kono Y, Greaux S, Higo Y, Ohfuji H, Irifune T (2010) Pressure and temperature dependences of elastic properties of grossular garnet up to 17 GPa and 1650 K. J Earth Sci 21(5):782–791. https://doi.org/10.1007/s12583-010-0112-2

Koornneef JM, Gress MU, Chinn IL, Jelsma HA, Harris JW, Davies GR (2017) Archaean and Proterozoic diamond growth from contrasting styles of large-scale magmatism. Nat Commun 8:648. https://doi.org/10.1038/s41467-017-00564-x

Kopylova MG, Gurney JJ, Daniels LRM (1997) Mineral inclusions in diamonds from the River Ranch kimberlite, Zimbabwe. Contrib Mineral Petrol 129(4):366–384. https://doi.org/10.1007/s004100050343

Kurat G, Dobosi G (2000) Garnet and diopside-bearing diamondites (framesites). Mineral Petrol 69(3):143–159. https://doi.org/10.1007/s007100070018

Leger J, Redon A, Chateau C (1990) Compressions of synthetic pyrope, spessartine and uvarovite garnets up to 25 GPa. Phys Chem Miner 17(2):161–167. https://doi.org/10.1007/BF00199668

Leitner BJ, Weidner DJ, Liebermann RC (1980) Elasticity of single crystal pyrope and implications for garnet solid solution series. Phys Earth Planet 22(2):111–121. https://doi.org/10.1016/0031-9201(80)90052-7

Levien L, Prewitt CT, Weidner DJ (1979) Compression of pyrope. Am Mineral 64(7–8):7–8

Locock AJ (2008) An Excel spreadsheet to recast analyses of garnet into end-member components, and a synopsis of the crystal chemistry of natural silicate garnets. Comput Geosci 34(12):1769–1780. https://doi.org/10.1016/j.cageo.2007.12.013

Mazzucchelli ML, Angel RJ, Alvaro M (2021) EntraPT: An online platform for elastic geothermobarometry. Am Mineral 106(5):830–837. https://doi.org/10.2138/am-2021-7693CCBYNCND

Meyer HOA, Svisero DP (1975) Mineral inclusions in Brazilian diamonds. Phys Chem Earth 9(Supplement C):785–795. https://doi.org/10.1016/0079-1946(75)90051-8

Milani S, Nestola F, Alvaro M, Pasqual D, Mazzucchelli ML, Domeneghetti MC, Geiger CA (2015) Diamond–garnet geobarometry: The role of garnet compressibility and expansivity. Lithos 227:140–147. https://doi.org/10.1016/j.lithos.2015.03.017

Milani S, Angel RJ, Scandolo L, Mazzucchelli ML, Ballaran TB, Klemme S, Domeneghetti MC, Miletich R, Scheidl KS, Derzsi M (2017) Thermo-elastic behavior of grossular garnet at high pressures and temperatures. Am Mineral 102(4):851–859. https://doi.org/10.2138/am-2017-5855

Miller CE, Kopylova MG, Ryder J (2012) Vanished diamondiferous cratonic root beneath the Southern Superior province: evidence from diamond inclusions in the Wawa metaconglomerate. Contrib Mineral Petrol 164(4):697–714

Miller CE, Kopylova M, Smith E (2014) Mineral inclusions in fibrous diamonds: constraints on cratonic mantle refertilization and diamond formation. Mineral Petrol 108(3):317–331

Nestola F (2021) How to apply elastic geobarometry in geology. Am Mineral 106(5):669–671. https://doi.org/10.2138/am-2021-7845

Ntanda FM, Moreau J, Meyer H (1982) Particularites des inclusions cristallines primaires des diamants du Kasai, Zaire. Can Mineral 20(2):217–230

Olijnyk H, Paris E, Geiger C, Lager G (1991) Compressional study of katoite [$Ca_3Al_2(O_4H_4)_3$] and grossular garnet. J Geophys Res 96(B9):14313–14318. https://doi.org/10.1029/91JB01180

O'Neill B, Bass JD, Smyth JR, Vaughan MT (1989) Elasticity of a grossular-pyrope-almandine garnet. J Geophys Res 94(B12):17819–17824. https://doi.org/10.1029/JB094iB12p17819

O'Neill B, Bass JD, Rossman GR, Geiger CA, Langer K (1991) Elastic properties of pyrope. Phys Chem Miner 17(7):617–621. https://doi.org/10.1007/BF00203841

Pavese A, Diella V, Pischedda V, Merli M, Bocchio R, Mezouar M (2001a) Pressure–volume–temperature equation of state of andradite and grossular, by high-pressure and -temperature powder diffraction. Phys Chem Miner 28(4):242–248. https://doi.org/10.1007/s002690000144

Pavese A, Levy D, Pischedda V (2001b) Elastic properties of andradite and grossular, by synchrotron X-ray diffraction at high pressure conditions. Eur J Mineral 13(5):929–937. https://doi.org/10.1127/0935-1221/2001/0013-0929

Phillips D, Harris JW, Viljoen KS (2004) Mineral chemistry and thermobarometry of inclusions from De Beers Pool diamonds, Kimberley, South Africa. Lithos 77(1):155–179. https://doi.org/10.1016/j.lithos.2004.04.005

Prencipe M, Bruno M, Nestola F, De La Pierre M, Nimis P (2014) Toward an accurate ab initio estimation of compressibility and thermal expansion of diamond in the [0, 3000 K] temperature and [0, 30 GPa] pressures ranges, at the hybrid HF/DFT theoretical level. Am Mineral 99(5–6):1147–1154. https://doi.org/10.2138/am.2014.4772

Prinz M, Vincent Manson D, Hlava PF, Keil K (1975) Inclusions in diamonds: Garnet lherzolite and eclogite assemblages. Phys Chem Earth 9(Supplement C):797–815. https://doi.org/10.1016/0079-1946(75)90052-X

Qi L, Tang Z, Lv X, He M, Zhang F, Miao Q (1999) Typomorphic peculiarities and significance of mineral inclusions in diamond in Liaoning Province, China (in Chinese). J Gems Gemmol 1(3):27–34

Rivers M, Prakapenka VB, Kubo A, Pullins C, Holl CM, Jacobsen SD (2008) The COMPRES/GSECARS gas-loading system for diamond anvil cells at the Advanced Photon Source. High Press Res 28(3):273–292. https://doi.org/10.1080/08957950802333593

Sato Y, Akaogi M, Akimoto S-I (1978) Hydrostatic compression of the synthetic garnets pyrope and almandine. J Geophys Res 83(B1):335–338. https://doi.org/10.1029/JB083iB01p00335

Schulze DJ, Coopersmith HG, Harte B, Pizzolato L-A (2008) Mineral inclusions in diamonds from the Kelsey Lake Mine, Colorado, USA: depleted Archean mantle beneath the Proterozoic Yavapai province. Geochim Cosmochim Acta 72(6):1685–1695

Shatsky VS, Zedgenizov DA, Ragozin AL, Kalinina VV (2015) Diamondiferous subcontinental lithospheric mantle of the northeastern Siberian Craton: Evidence from mineral inclusions in alluvial diamonds. Gondwana Res 28(1):106–120. https://doi.org/10.1016/j.gr.2014.03.018

Sinogeikin SV, Bass JD (2000) Single-crystal elasticity of pyrope and MgO to 20 GPa by Brillouin scattering in the diamond cell. Phys Earth Planet 120(1):43–62. https://doi.org/10.1016/S0031-9201(00)00143-6

Sinogeikin SV, Bass JD (2002) Elasticity of pyrope and majorite–pyrope solid solutions to high temperatures. Earth Planet Sci Lett 203(1):549–555. https://doi.org/10.1016/S0012-821X(02)00851-8

Skinner BJ (1956) Physical properties of end-members of the garnet group. Am Mineral 41(5–6):428–436

Sobolev NV, Logvinova AM, Zedgenizov DA, Seryotkin YV, Yefimova ES, Floss C, Taylor LA (2004) Mineral inclusions in microdiamonds and macrodiamonds from kimberlites of Yakutia: a comparative study. Lithos 77(1):225–242. https://doi.org/10.1016/j.lithos.2004.04.001

Sobolev NV, Logvinova AM, Efimova ES (2009) Syngenetic phlogopite inclusions in kimberlite-hosted diamonds: implications for role of volatiles in diamond formation. Russ Geol Geophys 50(12):1234–1248. https://doi.org/10.1016/j.rgg.2009.11.021

Stachel T, Harris JW (1997) Syngenetic inclusions in diamond from the Birim field (Ghana)—a deep peridotitic profile with a

history of depletion and re-enrichment. Contrib Mineral Petrol 127(4):336–352. https://doi.org/10.1007/s004100050284

Stachel T, Harris JW (2008) The origin of cratonic diamonds—constraints from mineral inclusions. Ore Geol Rev 34(1):5–32. https://doi.org/10.1016/j.oregeorev.2007.05.002

Stachel T, Harris JW, Brey GP (1998) Rare and unusual mineral inclusions in diamonds from Mwadui, Tanzania. Contrib Mineral Pet 132(1):34–47

Stachel T, Brey GP, Harris JW (2000) Kankan diamonds (Guinea) I: from the lithosphere down to the transition zone. Contrib Mineral Petrol 140(1):1–15. https://doi.org/10.1007/s004100000173

Stachel T, Harris JW, Tappert R, Brey GP (2003) Peridotitic diamonds from the Slave and the Kaapvaal cratons—similarities and differences based on a preliminary data set. Lithos 71(2):489–503

Stachel T, Aulbach S, Brey GP, Harris JW, Leost I, Tappert R, Viljoen KS (2004a) The trace element composition of silicate inclusions in diamonds: a review. Lithos 77(1):1–19. https://doi.org/10.1016/j.lithos.2004.03.027

Stachel T, Viljoen KS, McDade P, Harris JW (2004b) Diamondiferous lithospheric roots along the western margin of the Kalahari Craton—the peridotitic inclusion suite in diamonds from Orapa and Jwaneng. Contrib Mineral Petrol 147(1):32–47. https://doi.org/10.1007/s00410-003-0535-1

Stachel T, Banas A, Muehlenbachs K, Kurszlaukis S, Walker EC (2006) Archean diamonds from Wawa (Canada): samples from deep cratonic roots predating cratonization of the Superior Province. Contrib Mineral Petrol 151(6):737. https://doi.org/10.1007/s00410-006-0090-7

Suzuki I, Anderson OL (1983) Elasticity and thermal expansion of a natural garnet up to 1,000 K. J Phys Earth 31(2):125–138. https://doi.org/10.4294/jpe1952.31.125

Takahashi T, Liu L-G (1970) Compression of ferromagnesian garnets and the effect of solid solutions on the bulk modulus. J Geophys Res 75(29):5757–5766. https://doi.org/10.1029/JB075i029p05757

Tappert R, Stachel T, Harris JW, Muehlenbachs K, Ludwig T, Brey GP (2005a) Diamonds from Jagersfontein (South Africa): messengers from the sublithospheric mantle. Contrib Mineral Petrol 150(5):505–522

Tappert R, Stachel T, Harris JW, Shimizu N, Brey GP (2005b) Mineral inclusions in diamonds from the Panda kimberlite, Slave Province, Canada. Eur J Mineral 17(3):423–440

Tappert R, Stachel T, Harris JW, Muehlenbachs K, Brey GP (2006) Placer diamonds from Brazil: indicators of the composition of the earth's mantle and the distance to their kimberlitic sources. Econ Geol 101(2):453–470

Taylor LA, Anand M, Promprated P, Floss C, Sobolev NV (2003) The significance of mineral inclusions in large diamonds from Yakutia, Russia. Am Mineral 88(5–6):912–920. https://doi.org/10.2138/am-2003-5-621

Taylor LA, Logvinoya AM, Howarth GH, Liu Y, Peslier AH, Rossman GR, Guan YB, Chen Y, Sobolev NV (2016) Low water contents in diamond mineral inclusions: Proto-genetic origin in a dry cratonic lithosphere. Earth Planet Sci Lett 433:125–132. https://doi.org/10.1016/j.epsl.2015.10.042

Thieblot L, Roux J, Richet P (1998) High-temperature thermal expansion and decomposition of garnets. Eur J Mineral 10:7–15. https://doi.org/10.1127/ejm/10/1/0007

Viljoen KS, Harris JW, Ivanic T, Richardson SH, Gray K (2014) Trace element chemistry of peridotitic garnets in diamonds from the Premier (Cullinan) and Finsch kimberlites, South Africa: contrasting styles of mantle metasomatism. Lithos 208–209(Supplement C):1–15. https://doi.org/10.1016/j.lithos.2014.08.010

Wang Z, Guo G (1994) Characteristics of inclusions from diamond in No. 50 pipe at Wafangdian, South Liaoning. Liaoning Geol 3:263–274

Wang Z, Ji S (2001) Elasticity of six polycrystalline silicate garnets at pressure up to 3.0 GPa. Am Mineral 86(10):1209–1218. https://doi.org/10.2138/am-2001-1009

Wang Y, Weidner DJ, Zhang J, Gwanrnesia GD, Liebermann RC (1998) Thermal equation of state of garnets along the pyrope-majorite join. Phys Earth Planet 105(1):59–71. https://doi.org/10.1016/S0031-9201(97)00072-1

Wang W, Sueno S, Takahashi E, Yurimoto H, Gasparik T (2000) Enrichment processes at the base of the Archean lithospheric mantle: observations from trace element characteristics of pyropic garnet inclusions in diamonds. Contrib Mineral Pet 139(6):720–733

Weaver JS, Takahashi T, Bass J (1976) Isothermal compression of grossular garnets to 250 kbar and the effect of calcium on the bulk modulus. J Geophys Res 81(14):2475–2482. https://doi.org/10.1029/JB081i014p02475

Wei W, Mao Z, Sun N, Sun D, Tkachev SN (2021) High pressure-temperature single-crystal elasticity of grossular: implications for the low-velocity layer in the bottom transition zone. Geophys Res Lett. https://doi.org/10.1029/2021gl093540

Wiggers de Vries DF, Pearson DG, Bulanova GP, Smelov AP, Pavlushin AD, Davies GR (2013) Re–Os dating of sulphide inclusions zonally distributed in single Yakutian diamonds: Evidence for multiple episodes of Proterozoic formation and protracted timescales of diamond growth. Geochim Cosmochim Acta 120(Supplement C):363–394. https://doi.org/10.1016/j.gca.2013.06.035

Xu J, Zhang D, Fan D, Dera PK, Shi F, Zhou W (2019) Thermoelastic properties of eclogitic garnets and omphacites: implications for deep subduction of oceanic crust and density anomalies in the upper mantle. Geophys Res Lett 46(1):179–188. https://doi.org/10.1029/2018GL081170

Xu J, Zhang D, Tkachev SN, Dera PK (2022) Partnership for eXtreme Xtallography (PX^2)—a state-of-the-art experimental facility for extreme-conditions crystallography: A case study of pressure-induced phase transition in natural ilvaite. Matter Radiat Extremes 7(2):028401. https://doi.org/10.1063/5.0075795

Zedgenizov D, Rubatto D, Shatsky V, Ragozin A, Kalinina V (2016) Eclogitic diamonds from variable crustal protoliths in the northeastern Siberian craton: trace elements and coupled δ13C–δ18O signatures in diamonds and garnet inclusions. Chem Geol 422(Supplement C):46–59. https://doi.org/10.1016/j.chemgeo.2015.12.018

Zhang A (1991) Diamond prospecting indicative mineral research and database. Beijing Science and Technology Press, Beijing

Zhang L, Ahsbahs H, Kutoglu A (1998) Hydrostatic compression and crystal structure of pyrope to 33 GPa. Phys Chem Miner 25(4):301–307. https://doi.org/10.1007/s002690050118

Zhang L, Ahsbahs H, Kutoglu A, Geiger CA (1999) Single-crystal hydrostatic compression of synthetic pyrope, almandine, spessartine, grossular and andradite garnets at high pressures. Phys Chem Miner 27(1):52–58. https://doi.org/10.1007/s002690050240

Zhang D, Dera PK, Eng PJ, Stubbs JE, Zhang JS, Prakapenka VB, Rivers ML (2017) High pressure single crystal diffraction at PX^2. J vis Exp 119:e54660. https://doi.org/10.3791/54660

Zhang D, Chen M, Dera PK, Eng PJ (2021) Experimental calibration of the reduced partition function ratios of tetrahedrally coordinated silicon from the Debye-Waller factors. Contrib Mineral Petrol 176(9):66. https://doi.org/10.1007/s00410-021-01820-6

Zou Y, Irifune T (2012) Phase relations in $Mg_3Cr_2Si_3O_{12}$ and formation of majoritic knorringite garnet at high pressure and high

temperature. J Miner Petrol Sci 107(5):197–205. https://doi.org/10.2465/jmps.120318

Zou Y, Gréaux S, Irifune T, Whitaker ML, Shinmei T, Higo Y (2012a) Thermal equation of state of $Mg_3Al_2Si_3O_{12}$ pyrope garnet up to 19 GPa and 1,700 K. Phys Chem Miner 39(7):589–598. https://doi.org/10.1007/s00269-012-0514-z

Zou Y, Irifune T, Gréaux S, Whitaker ML, Shinmei T, Ohfuji H, Negishi R, Higo Y (2012b) Elasticity and sound velocities of polycrystalline $Mg_3Al_2(SiO_4)_3$ garnet up to 20 GPa and 1700 K. J Appl Phys 112(1):014910. https://doi.org/10.1063/1.4736407